Title

Stress transfer from rocking shallow foundations on soil-cement reinforced clay

Journal

Soils and Foundations, 59(4)

ISSN

0385-1621

Authors

Khosravi, Mohammad
Boulanger, Ross W
Wilson, Daniel W
et al.

Publication Date

2019-08-01

DOI

10.1016/j.sandf.2019.04.003

Peer reviewed

Stress Transfer from Rocking Shallow Foundations on Soil-Cement Reinforced Clay

by

Mohammad Khosravi, Assistant Professor
(Corresponding author: email: mkhosravi@montana.edu, phone: +1-7202890497)
(Address: 86 S Cottonwood Rd, Apt 201, Bozeman, MT, 59718)
Department of Civil Engineering
Montana State University, Bozeman, MT, 59718

Ross W. Boulanger, Professor
Department of Civil and Environmental Engineering
University of California, Davis, CA, 95616

Daniel W. Wilson, Associate Director
Center for Geotechnical Modeling, Department of Civil and Environmental Engineering
University of California, Davis, CA, 95616

C. Guney Olgun, Assistant Professor
Civil, Architectural and Environmental Engineering
Missouri University of Science and Technology, Rolla, MO, USA 65409

Lisheng Shao, Ph.D., P.E. G.E.
Hayward Baker Inc., Western Region, Santa Paula, CA, USA, 93060

Shuji Tamura, Professor
Department of Architecture and Building Engineering
Tokyo Institute of Technology, Tokyo, Japan

Author's version in June 2019 prior to copyediting, final edits,
and publication in the Soils and Foundations

Abstract.

Equivalent-static pushover analyses with a three-dimensional (3D), nonlinear, finite-difference model are used to investigate the static and seismic stresses imposed on soil-cement grid reinforcements in soft clay profiles by overlying structures supported on shallow footings. The goal is to evaluate potential stress concentrations in the soil-cement grid during foundation rocking and the potential for large foundation settlements associated with local crushing of the soil-cement. The numerical analyses are first validated using data from dynamic centrifuge experiments that included cases with and without large foundation settlements and localized crushing of the soil-cement grids. The experimental and numerical results indicate that the stresses imposed on the soil-cement grid by the overlying structure require accounting for foundation rocking during strong shaking and stress concentrations at the soil-cement grid intersections. The numerical analyses provide reasonable prediction of structural rocking loads and the zone of expected crushing or lack of crushing, but under-estimate the accumulation of foundation settlements when seismic demands repeatedly exceed the soil-cement strength. The simulated moment-rotation and uplift behavior of the footings under monotonic lateral loading are reasonably consistent with the dynamic centrifuge test results. Parametric analyses using the validated numerical model illustrate how stress transfer varies with the area replacement ratio, thickness of the top sand layer, properties of bearing sand layer, and relative stiffness of the soil-cement and surrounding soil. A design model for estimating the stresses imposed on a soil-cement grid by rocking foundations was developed and shown to provide a reasonable basis for assessing if local damage to the soil-cement grid is expected.

Keywords: *Soil-Cement Grid Reinforcement, Dynamic Response, Single Degree of Freedom System, Rocking Foundation, Dynamic Kinematic Loads.*

International Geotechnical Classification Numbers*: E08, E01, E12, E14*

Introduction

Soil-cement ground reinforcement is an in-situ soil stabilization technique that has been used for mitigation of earthquake-induced ground displacements and foundation settlements for a wide range of civil infrastructure systems (e.g., Kitazume and Terashi 2014, Bruce et al. 2013, Tokunaga et al. 2015). Previous studies of soil-cement reinforcement techniques, using case histories from past earthquakes (e.g. Tokimatsu et al. 1996, Yamashita et al. 2012, Tokunaga et al. 2015), dynamic centrifuge model tests (e.g. Adalier et al., 1998, Kitazume and Maruyama, 2006, Ishikawa and Asaka, 2006, Rayamajhi et al., 2014, Takahashi et al., 2006, Khosravi et al. 2016), and numerical analyses (e.g. Namikawa et al. 2007, Bradley et al. 2013, Nguyen et al. 2013, Puebla et al. 2006, Karimi and Dashti, 2016a,b), have shown the effectiveness of soil-cement ground reinforcement mitigation of earthquake-induced ground displacements. Most of these studies have evaluated overall deformation mechanisms and critical aspects of the seismic response of improved soil deposits subject to severe ground shaking. Few studies, however, have investigated the response of structures over soil-cement reinforced soil and the loading that these structures may impose on the soil-cement reinforcements.

Centrifuge experiments performed by Khosravi et al. (2015e, 2017) investigated the seismic response of single-degree-of-freedom (SDOF) structures with shallow foundations over soft soil reinforced with soil-cement grids. The onset of large foundation settlements during strong shaking coincided with rocking of the shallow foundations and localized cracking and crushing of the soil-cement under the footing edges. The rocking response and settlement of the structures were shown to depend on the area replacement ratio (A_r = area of soil-cement divided by total area), soil-cement strength, and intensity of the shaking motion. Design-oriented analyses of the centrifuge results further suggested that differentiating between conditions that did and did not cause

localized crushing of the soil-cement grids would require accounting for foundation rocking and possible stress concentrations in the soil-cement reinforcements (Khosravi et al. 2017).

This study uses equivalent-static pushover analyses with a three-dimensional (3D), nonlinear, finite difference model and dynamic centrifuge model test data to investigate the static and seismic stresses imposed on soil-cement grid reinforcements in soft clay profiles by overlying structures supported on shallow footings. The equivalent-static pushover analyses are used to evaluate the effects of structural inertial loading, and do not account for kinematic loading effects between the footings, soil, and soil-cement grids. The centrifuge model tests included a 23-m-thick (prototype) clay profile reinforced with soil-cement grids having area replacement ratios (A_r) of 24% and 33%. A bearing layer of coarse sand was placed over the grid-reinforced clay profile as a load transfer layer. Structures on square shallow foundations were placed over the central part of each soil-cement grid system. The equivalent static pushover analyses were first validated using the recorded responses of the structures and observed performance of the soil-cement grids during different shaking events. The pushover model was then used to evaluate how various parameters influence the stresses and stress concentrations in the soil-cement grid due to the rocking foundation loads. These parametric analyses included the area replacement ratio, thickness of the bearing sand layer between the footing and soil-cement grid, and the soil and soil-cement properties. A design-oriented analysis method for estimating the stresses imposed on the soil-cement grids was developed that reasonably approximates the results of the 3D pushover analyses. The simplified analysis method, combined with knowledge of the soil-cement strengths, provided a reasonable basis for evaluating potential damage to the soil-cement grid due to structural inertial loading.

Overview of Centrifuge Experiments

Two centrifuge tests were performed using the 9-m radius centrifuge at the University of California at Davis and the data archived for general distribution (Khosravi et al. 2015c, e, Khosravi et al. 2017). The tests consisted of two models, MKH02 and MKH04, as shown in Fig. 1. The centrifuge models examined a 23.4-m thick (prototype), lightly over-consolidated layer of kaolinite (Hydrite Flat DS) with three different soil-cement grid configurations: an "embedded" grid (EG) with A_r = 24%, an "embedded" grid with A_r = 33%, and a "floating" grid (FG) with A_r = 33%. The embedded grids penetrated the underlying dense sand layer, whereas the floating grid only extended half-way through the clay layer. A 2.2-m-thick (prototype) bearing layer of coarse Monterey sand was placed over the grid-reinforced clay profile. Properties of the kaolinite include: Liquid Limit, *LL*=47; Plastic Index, *PI*=19; specific gravity of solids, G_s=2.58; median particle size of 4.0 μm; and a coefficient of consolidation, C_v=0.7 mm^2/s in virgin loading and 2.3 mm^2/s in unloading/reloading (Khosravi et al. 2015a). A T-bar penetrometer was used as the primary tool for directly measuring the strength of the clay during the centrifuge test. Based on the T-bar test results, shown in Khosravi et al. (2015c,e), the undrained shear strength of the clay increased from about 10 kPa near the surface to about 61 kPa near the bottom. Unconfined compressive strengths for the soil-cement grid ($q_{u,sc}$) after 14 days of curing time were 480-650 kPa (average 580 kPa) and 675-1060 kPa (average 820 kPa) for MKH02 and MKH04, respectively (Khosravi et al 2015c,d).

The performance of the soil-cement grids was evaluated using twenty-six crack detectors embedded in the walls at the time they were formed. The crack detectors were 2-mm diameter pencil leads connected to a circuit by wires at each end (Tamura et al. 2018). These brittle conductors provide a binary indication of if, and when, cracking occurs. The pencil leads were oriented horizontally at different locations along the walls (Tamura et al. 2018).

Structures supported by square shallow foundations were placed over the central part of each soil-cement grid system in both MKH02 and MKH04 (Figs. 1a and 1b). The SDOF structures were comprised of aluminum square footings, aluminum rectangular hollow columns, and aluminum and steel block superstructures. The footing width and weight, superstructure weight, and height of the superstructure's center of mass from the footing base for all structures are summarized in Table 1. Sand was epoxied to the base of each footing to produce a rough interface. The models were subjected to 13 shaking events with peak base accelerations (PBAs) ranging from 0.006 to 0.546 g; the sequence and characteristics of each shaking event are described in Khosravi et al. (2017).

Dynamic Moment, Rotation, and Settlement Responses

Normalized moment-rotation and settlement-rotation plots for the footings on embedded grids with A_r = 24% (MKH02) and A_r = 33% (MKH04) during the strongest Kobe motion with PBA = 0.54 g are shown in Figs. 2a, and 2b, respectively. The footing moments, M_{ft}, are normalized by VL/2 (where V = structure weight, and L = footing width), which is the maximum possible restoring moment neglecting large deformation effects. The moment-rotation response of the footing on the grid with A_r = 33% showed one large cycle of rotation in each direction that mobilized the footing's peak moment capacity (M_{ft}) of about 95 MNm. The moment reduced slightly with increasing rotation beyond those at which M_{ft} was mobilized. The peak footing rotations were accompanied by an average vertical uplift of the footing (indicative of a rocking response), as shown in the plot of average vertical displacement versus footing rotation in Fig. 2b. The cyclic loading, however, resulted in accumulation of a permanent average footing settlement of 35 mm (with negligible residual tilt). The results of crack detectors and displacement transducers indicated no sign of damage in EG-A_r = 33%.

The dynamic response of the structure on the embedded grid with A_r = 24% in MKH02 during the strongest Kobe motion with PBA = 0.54g is also shown in Fig. 2a. The footing's moment capacity was also fully mobilized, and the peak rotations were almost two times greater than in MKH04 (i.e., 0.020 rad in Fig. 2a versus 0.01 rad in Fig. 2b). The superstructure experienced four successive acceleration cycles with maximum values of 0.50 g followed by many smaller cycles, as shown in Khosravi et al. (2017). The average footing settlement progressively increased to its final value of about 230 mm (Fig. 2a), which is almost seven times greater than in MKH04. This large settlement and residual rotation during the strongest Kobe motion are attributed to crushing of the soil-cement grid underneath the footing, as discussed below. The crack detectors also indicated that crushing of the soil-cement grid underneath the footing occurred during the strongest Kobe motion with PBA = 0.54 g.

The soil surrounding the soil-cement grids was excavated after completion of all shaking events and the cracking patterns in the grids mapped to document shaking-induced damage. Photographs of the embedded grids with A_r = 24% (MKH02) and A_r = 33% (MKH04) are shown in Figs. 3b and 3c, respectively. In MKH02, the soil-cement walls were extensively crushed beneath the structural footing (with crushing extending 0.3 to 0.5 m below the tops of the walls) and were significantly cracked to depths of up to 10 m (Fig. 3b). The crack orientations and locations were highly varied. In MKH04, the soil-cement walls showed no visible signs of crushing beneath the footings or cracking at larger depths (Fig. 3c).

Overview of Numerical Simulations

Three-dimensional nonlinear pushover analyses of the centrifuge tests were performed in the finite difference FLAC3D platform (Itasca 2012) to evaluate stress distributions in the soil-cement grids due to the rocking foundation loads. The soil and soil-cement were modeled with brick elements

(zones in FLAC3D) and a Mohr–Coulomb model in a total stress, uncoupled mode (no pore fluid). The selection of a simple versus more complex constitutive model depends on the purpose of the analyses and the sensitivity of the key response measures to the details of the soil properties and imposed loading. The Mohr–Coulomb model only approximately accounts for soil and soil-cement nonlinearity, but sensitivity analysis showed that the results and trends are not significantly affected by large changes in the stiffness assigned to the different materials. Similarly, pseudo-static pushover analyses cannot simulate many of the dynamic response details evident in nonlinear dynamic systems (experiment or analysis). Nonetheless, the present analyses are believed to provide an appropriate basis for developing a reasonably conservative design procedure for estimating the stresses transferred from the footings to the soil-cement grids for practice.

The soil and soil-cement parameters, including unit weight (γ), friction angle (ϕ'), cohesion intercept (c), shear modulus (G), and bulk modulus (K), considered in these analyses are listed in Table 1. The cohesion of the soil-cement material is assumed to be half of the unconfined compressive strength of the soil-cement material. The friction angle for the top dense Monterey sand was estimated as 40 degrees based on the confining stresses and relative density (Salgado, 2008). The shear moduli for all sand materials were assumed to be constant, except for in sensitivity analyses. Shear modulus of the soil-cement material was obtained based on the available correlations between unconfined compressive strength and elastic modulus ($E = 300 \times q_{u,cs}$) (Kitazume and Terashi 2014). Sensitivity studies later examine the effects of variations in each of the key material parameters.

The configurations of the baseline models for the MKH02 and MKH04 centrifuge tests are shown in Fig. 4, from which various parameters (e.g. thickness of the bearing sand layer, soil properties, footing dimensions) were varied. The baseline models consisted of a 23.4-m-thick layer

of clay with 2.2-m thick layers of dense sand above and below the clay. The 1.2-m wide soil-cement walls were spaced 9.8 m and 7.0 m center-to-center apart, for an average A_r = 24% and A_r = 33% in MKH02 and MKH04, respectively (Figs. 4a and 4b). The base of the finite difference mesh was fixed and the lateral boundaries were fixed horizontally and free vertically. The mesh size and the maximum unbalanced force at the grid points (i.e., error tolerance) were selected based on a series of parametric analyses to optimize accuracy and computation speed. Finer zones were used near the soil surface and structural footing where deformation gradients were greatest.

The structural model, shown in Fig. 5, was modeled using quadratic solid elements for the superstructure and footing and beam elements for the column. The structural materials were modeled as linear-elastic (consistent with observed responses) with the properties listed in Table 1. The footing was connected to the soil zones by interface elements having Mohr–Coulomb strengths equal to those of the underlying sand. For the static pushover analysis, a horizontal velocity is applied on the center of mass of the superstructure.

Numerical Results for Models MKH02 and MKH04

The simulated pushover responses of the structures on embedded grids with A_r = 24% (MKH02) and A_r = 33% (MKH04) during monotonic lateral loading to a superstructure displacement of 420 mm are shown in Fig. 6. The computed moment-rotation responses for both footings are shown in Figure 6a, along with the centrifuge test results for peak footing moment (M_{ft}) versus peak footing rotation (θ_{ft}) for both footings and all shaking events. The pushover analyses are consistent with the measured peak responses, showing that maximum normalized moments of $M_{ft}/(VL/2) \approx 0.90$ were mobilized at footing rotations of $\theta_{ft} \approx 0.006$ rad. The computed maximum shear stresses, τ_{max}, that developed in the soil-cement grids under both footings are plotted versus footing rotation in Fig. 6b. These maximum shear stresses occurred in the corner crossings of the

longitudinal and transverse walls beneath the outer corners of the rocking footing contact area. The values of τ_{max} in these "critical junctures" are normalized by half the unconfined compressive strength of the soil-cement. For the embedded grid with A_r = 24%, the $\tau_{max}/(q_{u,sc}/2)$ reached a peak value of 1.0 at $\theta_{ft} \approx 0.006$ rad (Fig. 6b) which corresponds to $M_{ft}/(VL/2) \approx 0.9$; the $\tau_{max}/(q_{u,sc}/2)$ remained equal to 1.0 at larger footing rotations because the soil-cement material was plastically yielding. For the embedded grid with A_r = 33%, the $\tau_{max}/(q_{u,sc}/2)$ reached a peak value of only about 0.9 even at a footing rotation of $\theta_{ft} \approx 0.012$ rad (Fig. 6b), indicating that the soil-cement material never yielded; note that nonlinearity in the response is attributed to yielding in the sand between the footing base and the soil-cement grid. The computed normalized vertical displacement at the center of each footing is plotted versus footing rotation in Fig. 6c. Both footings developed similar uplift rates with increasing footing rotation, consistent with rocking about small contact areas at the outer edges of the footings.

The pushover results are further compared with dynamic centrifuge test results for select shaking events in Fig. 7. Normalized moment-rotation and settlement-rotation plots for the footings on the embedded grid with A_r = 24% (MKH02) during the Kobe motion with PBA = 0.19 g and embedded grid with A_r = 33% (MKH04) during the strongest Kobe motion with PBA = 0.54 g are shown in Figs. 7a, and 7b, respectively. The measured responses show that the footings were loaded to their full moment capacities (upper halves of Figs. 7a and 7b) and that the peak footing rotations were accompanied by vertical uplift at the footing center, indicative of rocking on the outer edges of the footing (lower halves of Figs. 7a and 7b). In addition, the cumulative settlement of the footings remained small (less than 40 mm), which is consistent with the experimental data indicating that significant crushing of the soil-cement did not occur in these events. The pushover

results, shown as dashed lines in these figures, provide reasonable approximations of the footing rocking in the peak loading cycles (i.e., peak uplift at the peak rotation) in these shaking events, but do not capture the cumulative settlement associated with the reversed cyclic loading.

The pushover results are compared to the dynamic response of the structure on the embedded grid with A_r = 24% in MKH02 during the strongest Kobe motion with PBA = 0.54 g in Fig. 7c. The soil-cement experienced significant crushing in this stronger shaking event (Fig. 3b), resulting in a net settlement of 230 mm. The centrifuge results suggest that the strength of the soil-cement, number of strong cycles of footing rotation, and footing rotation amplitudes controlled the degree of soil-cement damage and settlement accumulation. The pushover results begin to over-estimate the moment-rotation resistance at large rotations and cannot approximate the cyclic accumulation of foundation settlements because the mechanism of soil-cement crushing is not included in the numerical model.

Stress Distribution under the Footing

The stresses imposed on the soil-cement grids by the overlying structure include static and dynamic components, both of which depend on: (1) the mechanism of load transfer from the footing through the sand to the elevation of the grid surface, (2) the distribution or sharing of stresses between the soil-cement grid and its surrounding soil, and (3) the distribution of stresses within the soil-cement grid.

The computed stress distribution under the footing for static loading under the weight of the structure alone is illustrated by the results in Fig. 8 for the baseline model with A_r = 24%. This figure shows 3D contours of the change in vertical stress ($\Delta\sigma_v$) imposed on the sand at the elevation of the footing base (Fig. 8a) and at the elevation of the soil-cement grid surface (Fig. 8b). The average $\Delta\sigma_v$ on the base of the footing (0.9 m below the ground surface), or the value of an

equivalent uniformly distributed stress, is 100.5 kPa (the gray area in Fig. 8a). Instead, the soil under the footing deflects in a bowl-shaped depression, relieving stresses under the middle of the footing. The $\Delta\sigma_v$ under the footing increases from 32 kPa beneath the footing center to a maximum of 184 kPa beneath the corners of the footing. The $\Delta\sigma_v$ at the elevation of the soil-cement grid surface (i.e., at a depth of 2.2 m below the footing base) is shown in Fig. 8b. Assuming a uniform stress distribution at this depth with stresses spreading at 2(vertical):1(horizontal) from the footing base (the gray area in Fig. 8b), the expected $\Delta\sigma_v$ would be 71 kPa. Instead, the $\Delta\sigma_v$ is only 32 kPa on the soil at the middle of the grid cell and reaches a maximum of 117 kPa at the corner juncture of the soil-cement grid. The concentration of $\Delta\sigma_v$ in the soil-cement grid junctures and in the sand overlying these junctures is attributed to both the greater stiffness of the soil-cement and the junctures providing a preferential location for loads to arch onto.

The computed stress distribution under the footing for the pseudo-static approximation of dynamic loading is shown in Fig. 9 for the same baseline model with $A_r = 24\%$ loaded to a peak $\theta_{ft} \approx 0.006$ rad (associated with $M_{ft}/(VL/2) \approx 0.90$). Contours of $\Delta\sigma_v$ at the footing base and on the top of the soil-cement grid are presented in Figs. 9a and 9b, respectively. Rotation of the footing reduced its contact area with the soil, thereby increasing stresses beneath the footing edge. On the footing base (Fig. 9a), the maximum $\Delta\sigma_v$ of 1050 kPa occurs at the corners directly over the soil-cement grid juncture whereas $\Delta\sigma_v$ is only 447 kPa at the middle of the footing edge (over a transverse wall in the soil-cement grid). At the top of the soil-cement grid (Fig. 9b), the maximum $\Delta\sigma_v$ of 470 kPa also occurs at the critical juncture of the soil-cement grid whereas $\Delta\sigma_v$ is only 302 kPa at the middle of the transverse wall. The $\Delta\sigma_v$ imposed on the soil inside the grids is almost zero at the middle of the grid, and increases to about 100 kPa near the grid walls. The maximum

$\Delta\sigma_v$ on the soil-cement grid under this rocking foundation load is four times greater than the maximum $\Delta\sigma_v$ under static loading alone (470 kPa in Fig. 9b versus 117 kPa in Fig. 8b), whereas the maximum $\Delta\sigma_v$ on the enclosed soil is about three times greater.

Parametric Analyses

Sensitivity to Sand Friction Angle

The effect of the sand layer's ϕ' on the pushover response of the structure and the stresses imposed on the footing base and soil-cement walls are presented in Fig. 10 for a model with A_r = 24% and H_s =2.2 m. Analyses were repeated with ϕ' of 35, 40 and 45 degrees, while all other parameters were kept constant. The footing moment versus rotation response is shown in Fig. 10a and the maximum shear stress in the soil-cement versus footing rotation is shown in Fig. 10b. Profiles of $\Delta\sigma_v$ directly over the longitudinal (EG-L) and transverse (EG-T) walls of the soil-cement grid when θ_{ft} = 0.006 rad (associated with $M_{ft}/(VL/2) \approx 0.90$) are shown in Figs. 10c and 10d, respectively; the $\Delta\sigma_v$ at the footing base are shown as dashed lines, whereas the $\Delta\sigma_v$ at the top of the soil-cement grid are shown as solid lines. Increasing the sand ϕ' from 35 to 45 degrees increased the moment capacity of the footing by only 10% (Fig 10a), while the maximum $\Delta\sigma_v$ at the footing base increased by about 65% (dashed lines in Fig. 10c and 10d). These results are consistent with the findings of Gajan and Kutter (2008) in indicating that the moment capacity of a rocking foundation on sand is well defined and relatively insensitive to a range of typical friction angles. The maximum shear stress in the soil-cement (Fig. 10b) and the maximum $\Delta\sigma_v$ imposed on the top of the soil-cement grid (solid lines in Figs. 10c and 10d) are insensitive to this range of friction angles because they are largely controlled by yielding in the soil-cement.

Sensitivity to Sand Layer Thickness

The effect of the sand layer thickness (H_s) on the pushover response of the structure and the stresses imposed on the footing base and soil-cement walls is illustrated by the results in Fig. 11 for a model with A_r = 24%, ϕ' =40 degrees, and H_s of 1.0 and 2.2 m. The footing moment versus rotation response is shown in Fig. 11a and the maximum shear stress in the soil-cement versus footing rotation is shown in Fig. 11b. Profiles of $\Delta\sigma_v$ directly over the longitudinal (EG-L) and transverse (EG-T) walls of the soil-cement grid when θ_{ft} = 0.006 rad (associated with $M_{ft}/(VL/2) \approx 0.90$) are shown in Figs. 11c and 11d, respectively. The moment-rotation response of the footing is relatively independent of the sand layer thickness (Fig. 11a), as is the maximum contact stress of about 1700 kPa beneath the footing base (Figs. 11c and 11d). The maximum $\Delta\sigma_v$ on the soil-cement grid, however, increased from 500 kPa for H_s = 2.2 m to 800 kPa for H_s = 1.0 m (Figs. 11c and 11d). For both H_s = 1.0 and 2.2 m, the maximum shear stress in the soil-cement reached the strength of the soil-cement material, but at different footing rotations (Fig. 11b). In the model with H_s = 1.0 m, yielding in the soil-cement first occurs at $\theta_{ft} \approx 0.002$ rad which corresponds to $M_{ft}/(VL/2) \approx 0.78$, whereas in the model with H_s = 2.2 m, it first occurs at $\theta_{ft} \approx 0.006$ rad (associated with $M_{ft}/(VL/2) \approx 0.90$).

Contours of strength/stress ratio in the soil-cement at a footing rotation of 0.006 rad are shown on the 3D views of the soil-cement grid in Fig. 12; results for H_s = 2.2 m, 1.5 m, and 1.0 m are shown in Figs. 12a, 12b, and 12c, respectively. The stress-strength ratio is a local indicator of the current stress state's proximity to failure and is computed as the maximum principal stress difference that would develop at failure if the material had its current minimum principle stress, divided by the current principal stress difference (Itasca 2016). Contours are limited to strength/stress ratios less than 1.3 to emphasize those zones where stresses exceed typical design

values for the factor of safety against crushing (Bruce et al. 2013). Yielding of the soil-cement (i.e. strength/stress ratio of 1.0) corresponds to the dark blue zones in these figures. For H_s = 2.2 m (Fig. 12a), yielding of the soil-cement occurs only at the corners of the grid junctures (intersection of transverse and longitudinal walls) beneath the footing corners. The strength/stress ratio reduces with depth, reaching 1.3 at a depth of 3.3 m from the top of the soil-cement grid. Reducing H_s to 1.5 m (Fig. 12b) and 1.0 m (Fig. 12c) caused the zones with strength/stress ratios less than 1.3 to extend to the larger depths of 4.7 m and 6.0 m, respectively. In addition, reducing H_s increased the extent of soil-cement yielding, with yielding extending to depths of 1.5 m in the transverse wall for the case with H_s = 1.0 (Fig. 12c). These simulation results suggest that crushing of the soil-cement starts at the corners of the grid junctures where stress concentrations develop under the rocking foundation loads. If yielding of the soil-cement was accompanied by strain-softening (which is not incorporated in the present analyses), stresses would be expected to redistribute from yielding zones onto other zones, contributing to a spreading of damage along the length of the transverse wall.

The τ_{max} in the highest-stressed zone of soil-cement are plotted versus H_s for models with A_r = 24% in Fig. 13a and A_r = 33% in Figs. 13b for footing rotations of 0.006 rad. Results are shown for sand ϕ' of 35, 40 and 45 degrees. For the grid with A_r = 24%, the τ_{max} is 300 kPa regardless of H_s or ϕ' because the soil-cement is yielding in all these cases. For the grid with A_r = 33%, the τ_{max} reduces from 395–410 kPa for H_s = 1.0 m to 260–305 kPa for H_s = 2.2 m. The average factor of safety against soil-cement crushing is 1.43 for H_s = 2.2 m suggesting that no crushing would be expected regardless of the sand ϕ'. The results in Fig. 13 are consistent with the previously discussed centrifuge test results, wherein crushing of soil-cement was observed in MKH02 with

A_r = 24% and $q_{u,cs}/2$ = 290 kPa (Fig. 3b), but not in MKH04 with A_r = 33% and $q_{u,cs}/2$ = 410 kPa (Fig. 3c).

Sensitivity to Stiffness Ratio

The effect of the relative stiffness of the soil-cement and enclosed soil on the stress transfer to the soil-cement grids is illustrated in Fig. 14, showing profiles of $\Delta\sigma_v$ along the tops of both the transverse and longitudinal walls for a model with A_r =24% and H_s = 2.2 m loaded to a footing rotation of 0.006 rad. The first analysis used the baseline soil and soil-cement properties listed in Table 1, such that the ratio of the soil-cement shear modulus (G_{sc}) to the enclosed soil's shear modulus (G_s) was 8.6. A second analysis was performed with G_{sc} increased by a factor of 5, producing a G_{sc}/G_s ratio of 43.5. The five-fold increase in G_{sc}/G_s produced only a 6% increase in the maximum $\Delta\sigma_v$ on the soil-cement grid. In either case, it appears that the grid was sufficiently stiff, relative to the enclosed soil, to carry the majority of the overlying structure's loads.

Other Sensitivity Analyses

Other sensitivity analyses examined various details of the numerical modeling procedures and confirmed that the responses were insensitive to them. These analyses included coarsening the mesh (zone dimensions approximately doubled), using a Cam Clay model for the soft clay, and using stress-dependent moduli for the top sand layer. The effects of these variations on the stress distributions and key response measures were all negligible, which is consistent with the other sensitivity analysis results showing relatively modest effects of fairly large changes in the key soil properties.

Development of a Simplified Procedure

A simplified procedure to estimate the maximum shear stress in the soil-cement grid and potential for crushing of the soil-cement was developed based on the results of a second set of 3D numerical

simulations. These simulations used the same models as described in the previous section, except that the soil-cement materials were kept elastic. Development of the simplified procedure is based on: (1) examining the stress states in the soil-cement grid to determine the relative importance of different stress components, (2) developing a simple procedure for estimating the equivalent-uniform or average vertical stresses imposed on the top of the soil-cement grid, (3) developing stress concentration ratios that relate the maximum stresses imposed on the soil-cement to those computed by the equivalent-uniform procedure, and (4) combining the above steps into a procedure for estimating maximum shear stresses in the soil cement and evaluating it against the results of the 3D pushover analyses. Each of these steps are discussed below.

State of Stresses in the Soil-Cement

The stress states for four zones at different locations along the top of the soil-cement grid are shown as Mohr circles in Fig. 15 for the baseline model with A_r = 24% and H_s = 2.2 m at three different times; initial static conditions without a structure, under the static weight of the structure, and with the structure loaded laterally to a footing rotation of 0.006 rad. The four soil-cement zones are located at the middle of the critical juncture (Fig. 15a), corner of the critical juncture (Fig. 15b), center of the transverse wall (Fig. 15c), and edge of the transverse wall midway between junctures (Fig. 14d). The stresses are small prior to placement of a structure (black circles), but grow significantly under the static weight of the structure (red circles). The Mohr circles grow even more dramatically under the rocking foundation loads (blue circles). The role of vertical (σ_v) and horizontal shear (τ_h) stresses coming from the structural loading varied with location along the wall (e.g., on the transverse wall versus critical juncture) and position within the walls (e.g., center versus edge at either location). For the most strongly loaded zone in the critical juncture (Fig. 15b), the σ_v increased from 50 kPa without a structure to 638 kPa with the rocking foundation loads,

while the τ_h simultaneously increased from 0 to 60 kPa. The change in τ_h due to foundation loading is much smaller than the change in σ_v, which is attributed to the differences in how these stress components spread with depth and the fact that some of the horizontal loads on the structure were carried by lateral earth pressures against the sides of the footing. The results for the other three locations similarly show that the change in σ_v has a dominant effect of the size of the Mohr circles under foundation loading. The results for all locations also show the minor principle stress becomes slightly negative during foundation rocking. With these observations, it appears that the value of τ_{max} (i.e. the radius of the Mohr circle) that develops in the soil-cement under rocking foundation loads can be estimated as simply $\sigma_v/2$ with less than a 7% - 15% error for the critical juncture (average or maximum values) and transverse wall (albeit on the unconservative side).

Estimating Equivalent Uniform or Average Vertical Stresses on the Grid

The maximum footing contact stress and contact area under a rocking footing are controlled by the soil bearing capacity, footing geometry, and structure weight (e.g., Deng et al. 2012). If the maximum footing contract stress is uniformly distributed (as assumed in Fig. 16), the footing moment capacity for a rectangular footing rocking in one direction can be estimated as:

$$M_{c,ft} = V\frac{L}{2}\left(1 - \frac{L_{cs}}{L}\right) \quad (1)$$

where L = footing length, L_{cs} = length of footing contact area on the soil, and V = total weight of the structure (assumed to act at the centroid of the footing). The minimum value of L_{cs} occurs when the limit bearing capacity of the foundation soil (q_{bLc}) is fully mobilized, such that:

$$L_{cs} = \frac{V}{B_{cs}q_{bLc}} \quad (2)$$

where B_{cs} = width of the footing contact area on the soil.

For cases where the thickness of the sand layer between the footing base and soil-cement grid is sufficiently large, the q_{bLc} on the sand for vertical loading can be estimated from conventional bearing capacity formulae (e.g., Salgado 2008) as:

$$q_{bLc} = S_q d_q q_o N_q + 0.5 S_\gamma d_\gamma \gamma L_{cs} N_\gamma \quad (3)$$

where q_o is the surcharge beside the footing, N_q and N_γ are bearing factors, s_q and s_γ are shape factors, d_q and d_γ are depth factors, and L_{cs} is the length of the contact area. If the L_{cs} computed using the q_{bLc} from Equation (3) is less than the thickness of the sand layer, then the L_{cs} and q_{bLC} values are assumed to be reasonable estimates. Based on the properties in Table 1, the L_{cs} are 1.10 and 0.97 m for the grid with A_r = 24% (MKH02) and the grids with A_r = 33% (MKH04), respectively. The omission of inclination factors for estimating the q_{bLc} for a rocking footing follows prior research findings (e.g., Deng et al. 2012) and is conservative for estimating the stresses transferred to the soil-cement grid. The average $\Delta\sigma_v$ transmitted to the soil-cement grid for this case [i.e., sand layer thickness greater than the L_{cs} using the q_{bLc} from Equation (3)] was computed based on two assumptions: (1) the footing contact stress spreads at a 2V:1H slope down to the top of the grid, and (2) all vertical stress is transferred to the grid alone, with the enclosed soil not carrying any stress, as shown in Fig. 16. The average $\Delta\sigma_v$ transmitted to the top of the grid thus become the total structure weight divided by the soil-cement area within the 2V:1H spreading zone. For the geometry in Fig. 16, the equation to estimate $\Delta\sigma_v$ becomes,

$$\Delta\sigma_{v,2:1method} = \frac{V}{(B_{cs}+H_s)t_p + 2(L_{cs}+H_s-t_p)t_p} \quad (4)$$

where t_p = thickness of the soil-cement walls or panels.

For cases where the sand layer is relatively thin, it is assumed that the footing contact stresses are not limited by yielding in the sand but rather arch through the sand layer onto the grid without

any spreading (as illustrated in Fig. 17). This condition is assumed to apply whenever the L_{cs} computed using the q_{bLc} from Equation (3) is greater than the sand layer thickness. The maximum footing contact stress is then controlled by crushing of the soil-cement, such that $q_{bLc} = q_{u,cs}$. This approach likely over-estimates the increase of q_{bLc} with decreasing sand layer thickness, but this approximation seems appropriately conservative for evaluating performance of the soil cement grids. The equation for estimating the footing's moment capacity for this case is modified to:

$$M_{c,ft} = V\left(\frac{L}{2} - C_{Ac}\right) \quad (5)$$

where C_{Ac} = centroid of the critical contact area of the footing required to support the vertical load (i.e., the hatched area in Fig. 12). Here it is also assumed that all vertical stress is transferred to the grid alone, with the enclosed soil not carrying any stress. The base shear coefficient for rocking becomes:

$$C_r = \frac{1}{H_{St}}\left(\frac{L}{2} - C_{Ac}\right)\left(1 + \frac{m_{Ft}}{m_{St}}\right) \quad (6)$$

For the geometry in Fig. 17, the equation to estimate $\Delta\sigma_v$ becomes,

$$\Delta\sigma_v = \frac{V}{A_{Hatched}} \quad (7)$$

where $A_{Hatched}$ = estimated contact area between the footing and the soil-cement walls or panels.

Stress Concentration Ratios

The concentration of $\Delta\sigma_v$ at different locations along the top of the soil-cement grid, as observed in the 3D pushover analyses (e.g., Fig. 9), can now be expressed relative to the average (or equivalent uniform) $\Delta\sigma_v$ from the above-described procedure. Stress concentration ratios (SCRs) for three locations on the soil-cement grid are presented: (1) ratio of maximum $\Delta\sigma_v$ on the critical juncture to the average $\Delta\sigma_v$ on the grid, CJ_{max}, (2) ratio of average $\Delta\sigma_v$ on the critical juncture to the average $\Delta\sigma_v$ on the grid, CJ_{ave}, and (3) ratio of average $\Delta\sigma_v$ on the middle of the

transverse wall to the average $\Delta\sigma_v$ on the grid, TW_{ave}. The SCRs are plotted versus H_s for embedded grids with A_r =24% and 33% in Figs. 18a and 18b, respectively. For the grid with A_r = 24% (Fig. 18a), the CJ_{max}, CJ_{ave}, and TW_{ave} decrease slightly as H_s increases from 1.0 m to 2.2 m, but on average were about 1.8 (range of 1.61 – 1.93), 1.3 (range of 1.23 – 1.35), and 0.9 (range of 0.85 – 0.93), respectively. The values of CJ_{max} were about 30-40% greater than the CJ_{ave}, illustrating that the significant stress concentration in the corner of the grid junctures for this relatively low A_r value. For the grid with A_r = 33% (Fig. 18b), the differences in the stress concentration factors CJ_{max} and CJ_{ave} were smaller and all three SCRs were closer to unity when H_s = 2.2 m, indicating that stress concentration effects were smaller than for the A_r =24% case.

Combined Procedure

The maximum shear stress at different locations along the top of the soil-cement grid (e.g., in the critical juncture or along the transverse wall) can now be estimated as,

$$\tau_{max} = \frac{1}{2}\left(\sigma_{vo} + SCR \cdot \Delta\sigma_{v,2:1method}\right) \quad (1)$$

where σ_{vo} = total vertical stress without the structure, and *SCR* = the stress concentration ratio of interest. In this equation, the $\Delta\sigma_v$ is added to σ_{vo} to obtain an estimate of the total vertical stress (σ_v) on the soil-cement, which is then divided by two to estimate τ_{max} as discussed previously. Soil-cement crushing is expected when τ_{max} exceeds the strength of the soil-cement material, $q_{u,cs}/2$.

The analytical results obtained using this simplified procedure are compared to the results from the 3D pushover analyses in Fig. 19 for grids with A_r = 24% (Fig. 18a) and A_r = 33% (Fig. 19b) for H_s of 1.0 to 2.2 m and the structure loaded to footing rotation of 0.006 rad (mobilizing the full footing moment capacity). The SCR values for the critical juncture (CJ_{max} and CJ_{ave}) and transverse

wall (TW_{ave}) were taken from Fig. 19. All other parameters used the baseline values listed in Table 1. In this figure, the simplified procedure results are shown as curves and the 3D pushover results are shown as symbols. For the grid with A_r = 24% (Fig. 19a), τ_{max} from the simplified method were 15-35% greater than the 3D pushover results for the critical juncture (average or maximum values) and transverse wall. The overestimation of τ_{max} at all three locations is attributed to the simplified procedure over-estimating the $\Delta\sigma_v$ transmitted to the top of the grid, which more than compensated for the slightly unconservative approximation of τ_{max} as simply $\sigma_v/2$ (i.e. Fig. 14). For the grid with A_r = 33% (Fig. 19b), τ_{max} from the simplified procedure were 4-25% greater than the 3D pushover results for all three locations. The simplified procedure was slightly more conservative for the A_r = 24% cases, which is attributed to the effect of assuming the enclosed soil carries no vertical load (which becomes more significant at lower A_r values). Overall, the simplified procedure provides an appropriately conservative estimate of τ_{max} in the soil-cement, given the various other approximations required for design practice.

The simplified analysis results in Fig. 19 are consistent with the observed performance of the embedded soil-cement grids in the centrifuge tests MKH02 and MKH04, both of which had H_s = 2.2 m. For the grid with A_r = 24% (MKH02), the τ_{max} in the critical juncture was 400 kPa on average and 560 kPa in the most strongly loaded corner, both of which significantly exceed the soil-cement's shear strength of 300 kPa for this test. Thus, the critical juncture would be expected to experience extensive crushing damage. The estimated τ_{max} in the transverse wall (280 kPa) is slightly lower than the soil-cement shear strength, but any loss of load carrying capacity in the critical junction would transfer loads to the transverse walls, such that crushing would reasonably be expected to progress there as well. Thus, these results are consistent with the crushing observed

during model excavation (Fig. 3b). For the embedded grid with A_r = 33% (MKH04), the τ_{max} in the critical juncture was 314 kPa on average and 351 kPa in the most strongly loaded corner, both of which are significantly smaller than the soil-cement's shear strength of 410 kPa for this test. Therefore, crushing of the soil-cement would not be expected for the grid with A_r = 33% (MKH04) which was consistent with the absence of observed damage during post-test excavation (Fig. 3c).

The proposed procedure for evaluating the effects of structural inertial loading on soil-cement grids has been developed from a relatively narrow set of conditions, such that additional analyses or experiments should be performed before extending it to the broader set of conditions encountered in practice. Nonetheless, the results of this initial study illustrate that relatively simple models can be used to differentiate between situations where extensive crushing of the soil-cement would or would not be expected. In addition, these initial results illustrate that allowance needs to be made for stress concentrations in the soil-cement grids and that the magnitude of these stress concentrations reduces as the area replacement ratio increases and the thickness of the overlying soil layer increases.

Conclusion

Equivalent-static pushover analyses with a three-dimensional (3D), nonlinear, finite-difference model were used to investigate the static and seismic stresses imposed on soil-cement grid reinforcements in soft clay profiles by overlying structures supported on shallow footings. These numerical analyses were first validated using data from dynamic centrifuge experiments that included cases with and without large foundation settlements and localized crushing of the soil-cement grids. The 3D pushover analyses were shown to reasonably predict the foundation moment-rotation responses and patterns of damage observed in the centrifuge experiments.

A simple design-oriented procedure was developed for estimating the potential for soil-cement crushing damage due to the inertial response of the overlying structure. The proposed procedure utilizes: traditional bearing capacity formula to determine contact stresses and contact areas under a rocking footing; 2V:1H stress spreading from the footing base to the top of the soil-cement grid; stress-concentration factors for different locations on the grid; and a simple approximate of the complex state of stresses in the soil-cement. The procedure was shown to provide an appropriately conservative estimate of stress demands imposed on the soil-cement grids, considering the other approximations required for design practice, for the range of conditions covered by the 3D analyses and centrifuge model tests. Further analyses or experiments are required before extending the procedure to the broader set of conditions encountered in practice.

Acknowledgements

Support for this work was provided by the National Science Foundation (NSF) through the George E. Brown, Jr. Network for Earthquake Engineering Simulation (NEESR) under Grant No. CMMI-1208117, the Pacific Earthquake Engineering Research Center (PEER), and Hayward Baker, Inc. Any opinions or conclusions expressed herein are those of the authors and do not necessarily reflect the views of any of the above organizations. The authors appreciate the assistance of Dr. Lisheng Shao of Hayward Baker and the staff of the Center for Geotechnical Modeling at UC Davis.

References

Adalier, K., Elgamal, A. K., and Martin, G. R. (1998). "Foundation Liquefaction Countermeasures for Earth Embankments." *J. of Geotech. and Geoenviron. Eng.*, 124(6), 500-517.

Bradley, B.A., Araki, K., Ishii, T. and Saitoh, K. (2013). "Effect of lattice-shaped ground improvement geometry on seismic response of liquefiable soil deposits via 3-D seismic

effective stress analysis." *Soil Dynamics and Earthquake Eng.,* 48. 35-47.

Bruce, M.E.C., Berg, R.R., Collin, J.G., Filz, G.M., Terashi, M., and Yang D.S. (2013). "Deep Mixing for Embankment and Foundation Support." Report No. FHWA-HRT-13-046, Federal Highway Administration, Washington, DC.

Gajan, S., and Kutter, B. L. (2008). "Capacity, Settlement, and energy dissipation of shallow footings subjected to rocking." *J. Geotech. Geoenviron. Eng.,* 134(8): 1129-1141, DOI: https://doi.org/10.1061/(ASCE)1090-0241(2008)134:8(1129).

Ishikawa, A., and Asaka, Y. (2006). "Seismic responses of column and grid-type improved grounds. Physical modelling in geotechnics." *ICPMG '06 International conference; 6th, Physical modelling in geotechnics*, ICPMG '06, 521-526

Itasca 2016. FLAC3D, Fast Lagrangian Analysis of Continua in 3D dimensions, User's Guide, Version 5.01. Itasca Consulting Group, Inc., Minneapolis, MN.

Khosravi, M., Wilson, D. W., Boulanger, R. W., Olgun, C. G., Tamura, S., Wang, Y., Rayamajhi, D., (2015a). "1-m Radius Centrifuge Experiments: Seismic response of soft soil reinforced with soil-cement grid-Construction procedure," *Network for Earthquake Engineering Simulation (distributor)*, Dataset, doi:10.4231/D3DN3ZX1Q.

Khosravi, M., Tamura, S., Boulanger, R. W., Wilson, D. W., Olgun, C. G., Rayamajhi, D., Wang, Y. (2015b). "Dynamic Centrifuge Tests on Soft Clay Reinforced by Soil-Cement Grids." *IFCEE 2015*, 2349-2358, doi 10.1061/9780784479087.218.

Khosravi, M., Wilson, D. W., Boulanger, R. W., Olgun, C. G., Tamura, S., Wang, Y. (2015c). "Test MKH01: Dynamic Centrifuge Tests of Soft Clay Reinforced by Soil-Cement Grids," *Network for Earthquake Engineering Simulation (distributor),* Dataset, doi:10.4231/D3HD7NT63

Khosravi, M., Boulanger, R. W., Wilson, D. W., Tamura, S., Olgun, C. G., Wang, Y., (2015d). "Seismic Performance of Soil-Cement Grid Supporting a Structure over Soft Clay." *The Deep Mixing 2015 Conference,* San Francisco, CA, 631-640.

Khosravi, M., Wilson, D. W., Boulanger, R. W., Olgun, C. G., Tamura, S., Wang, Y., (2015e). "Test MKH02: Dynamic Centrifuge Tests of Structures on Soft Clay Reinforced by Soil-Cement Grids", *Network for Earthquake Engineering Simulation (distributor),* Dataset, doi:10.4231/D38P5VB1Q

Khosravi, M., Boulanger, R. W., Wilson, D. W., Tamura, S., Olgun, C. G., Wang, Y., (2016)." Dynamic Centrifuge Tests of Soft Clay Reinforced by Soil-Cement Grids." *J. Geotech. Geoenviron. Eng.,* 142(7): 04016027, DOI: 10.1061/(ASCE)GT.1943-5606.0001487.

Khosravi, M., Boulanger, R. W., Wilson, D. W., Olgun, C. G., Tamura, S., Wang, Y., (2017)." Dynamic Centrifuge Tests of Structures with Shallow Foundations on Soft Clay Reinforced by Soil-Cement Grids." *Soils and Foundations,* 57(4): 04016027, 501-513, DOI: 10.1016/j.sandf.2017.06.002.

Kitazume, M. and Maruyama, K. (2006). "External stability of group column type deep mixing improved ground under embankment." *Soils and Foundations*, 16(3), 323-340.

Kitazume, M. and Terashi, M. (2014). "The Deep Mixing Method." Tayler & Francis Group, London, UK, 410 p.

Namikawa, T., Koseki, J., Suzuki, Y. (2007). "Finite element analysis of lattice-shaped ground improvement by cement-mixing for liquefaction mitigation." *Soils and Foundations*, 47(3), 559–76.

Nguyen, T. V., Rayamajhi, D., Boulanger, R. W., Ashford, S. A., Lu, J., Elgamal, A., and Shao, L. (2013). "Design of DSM Grids for Liquefaction Remediation." *J. Geotech. Geoenviron.*

Eng., 140(3), 1923-1933.

Puebla, H., Butler, R.C., O'Neill, E.S., and Williams, R.R. (2006). "Static and Seismic Stress-Deformation Analyses of a Deep Soil Mix Wall." *4th International FLAC Symposium on Numerical Modeling in Geomechanics*, Madrid, Spain.

Rayamajhi, D., Tamura, S., Khosravi, M., Boulanger, R.W., Wilson, D., Ashford, S.A., and Olgun, C.G. (2014). "Dynamic Centrifuge Tests to Evaluate Reinforcing Mechanisms of Soil-Cement Columns in Liquefiable Sand." *J. Geotech. Geoenviron. Eng.,* 140(3), 04015015-1.

Salgado, R., (2008). "The Engineering of Foundations." McGraw-Hill, 888p.

Takahashi, H., Kitazume, M., Ishibashi, S. (2006). "Effect of deep mixing wall spacing on liquefaction mitigation." *Proc. of the 6th international conference on physical modelling in geotechnics*, 585-590.

Tamura, S., Khosravi, M., Wilson, D. W., Rayamajhi, D., Boulanger, R. W., Olgun, C. G., Wang, Y., (2018). "Simple method for detecting cracks in soil–cement reinforcement for centrifuge modelling", International Journal of Physical Modelling in Geotechnics, 0 0:0, 1-9, https://doi.org/10.1680/jphmg.17.00036.

Tokimatsu, K., Mizuno, H., Kakurai, M. (1996). "Building damage associated with geotechnical problems." *Soils and Foundations*, special issue on Geotechnical Aspects of the January 17, 1995 Hyogoken-Nambu Earthquake, 1, 219-234.

Tokunaga, S., Kitazume, M., Morikawa, Y., Takahashi, H., Nagatsu, T., Honda, N., Onishi, T., Asanuma, T., Kubo, S., Higashi, S. (2015). "Performance of cement deep mixing method in 2011 tohoku earthquake." *The Deep Mixing 2015 Conference*, San Francisco, CA, 1071-1080.

Yamashita, K., Hamada, J., Onimaru, S., Higashino, M., (2012). “Seismic behavior of piled raft with ground improvement supporting a base-isolated building on soft ground in Tokyo." *Soils and Foundations*, 52(5), 1000–1015.

Table 1. Parameters for the soil, soil-cement, and structures in the baseline models

Parameter	EG in MKH02	EG in MKH04
Upper sand layer		
Friction angle (ϕ')	40	40
Unit weight	17 kN/m^3	17 kN/m^3
Shear modulus (G)	30 MPa	30 MPa
Bulk modulus (K)	78 MPa	78 MPa
Clay layer		
Average undrained shear strength (S_u)	33 kPa	33 kPa
Unit weight	18.3kN/m^3	18.3kN/m^3
Shear modulus (G)	8.1 MPa	8.1 MPa
Bulk modulus (K)	78.3 MPa	78.3 MPa
Soil-cement		
Area replacement ratio, A_r (%)	24	33
Panel spacing, S (m)	6.9	9.8
Panel thickness, t_p (m)	1.2	1.2
Shear modulus (G)	70 MPa	70 MPa
Bulk modulus (K)	93 MPa	93 MPa
UCS of soil-cement, $q_{u,cs}$ (kPa)	600	820
Structure		
Footing width, L (m)	11.4	14.8
Superstructure weight, V_{st} (kN)	8658	8658
Footing weight, V_{ft} (kN)	3835	5866
Column weight, V_{col} (kN)	307	307
Height of V_{st} from footing base, H_{st} (m)	13.96	13.96
Height of V_{ft} from footing base, H_{ft} (m)	0.59	0.53
Height of V_{col} from footing base, H_{col} (m)	6.59	6.59
Column cross-sectional area, A_c (m^2)	1.048	
Column moment of inertia, I_x & I_y (kNm^2)	0.175 & 0.569	
Column Young's Modulus, E (kPa)	6.89×10^7	

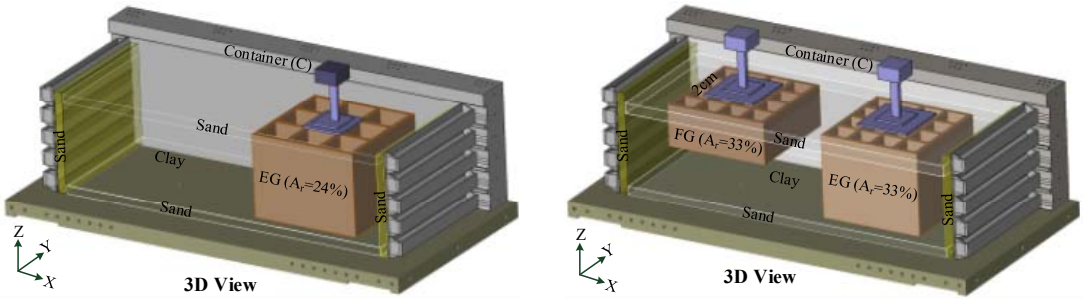

Fig. 1. Centrifuge model configurations: (a) MKH02 with an embedded grid having A_r = 24%, (b) MKH04 with floating and embedded grids having A_r = 33%.

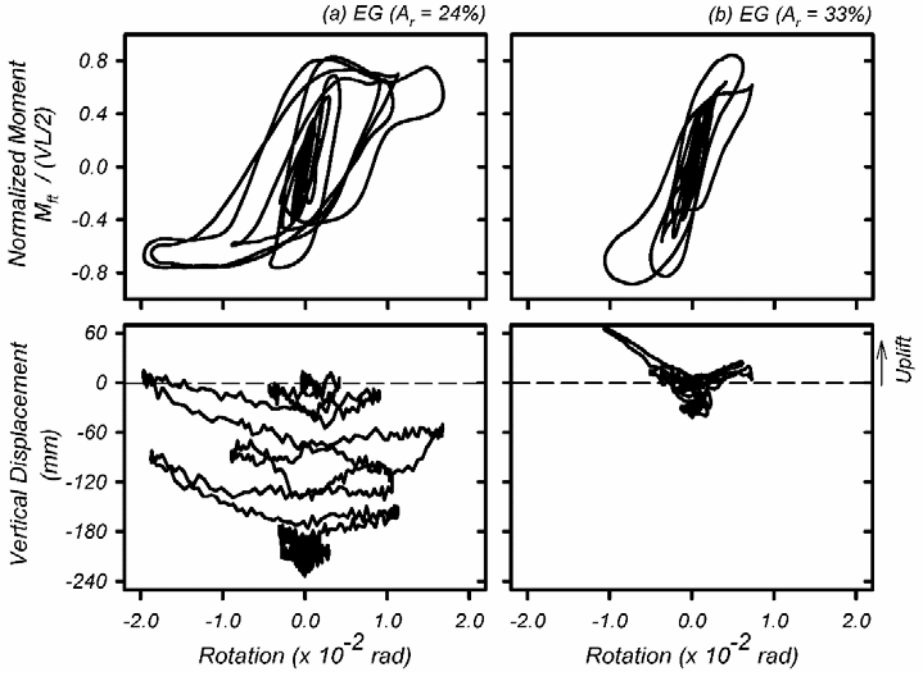

Fig. 2. Dynamic response of the structures located on the embedded grids (EG) during a Kobe motion with PBA = 0.54g, (a) response in MKH02 with A_r = 24%, and (b) response in MKH04 with A_r = 33%.

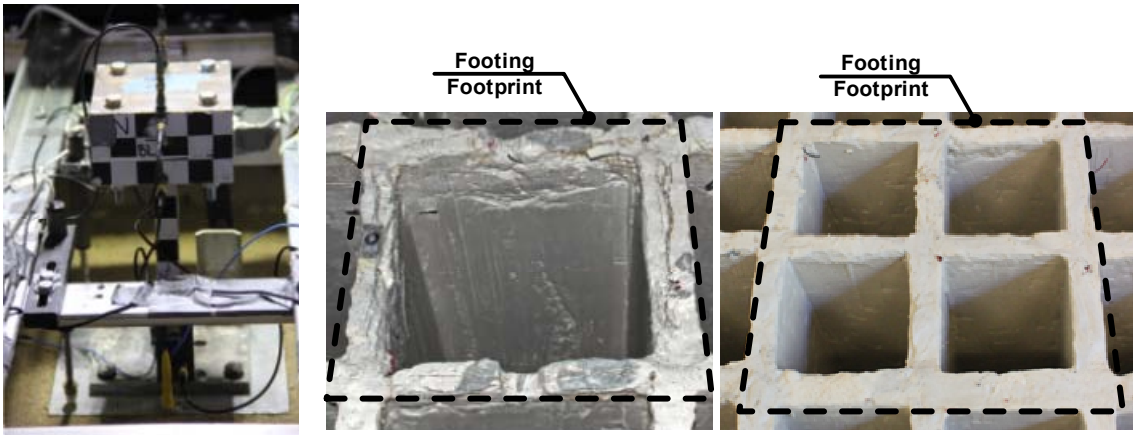

Fig. 3. Photographs from the centrifuge model tests: (a) a structural model before shaking, (b) soil-cement grid in MKH02 during post-test excavation, and (c) soil-cement grid in MKH04 during post-test excavation.

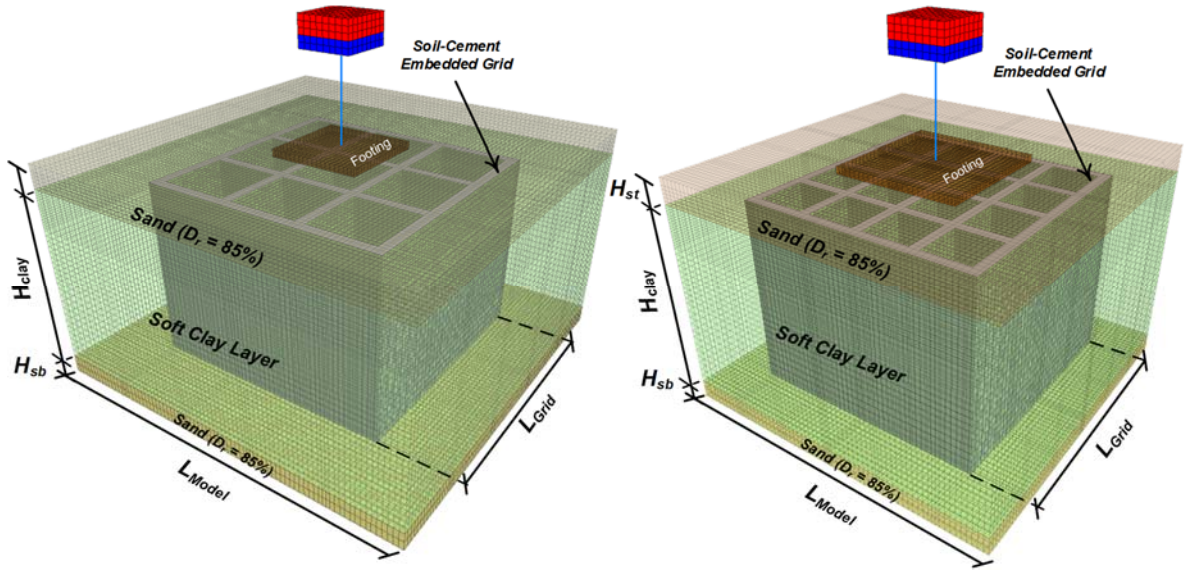

Fig. 4. Numerical model configurations: (a) the embedded grid with A_r = 24% in MKH02; and (b) the embedded grid with A_r = 33% in MKH04.

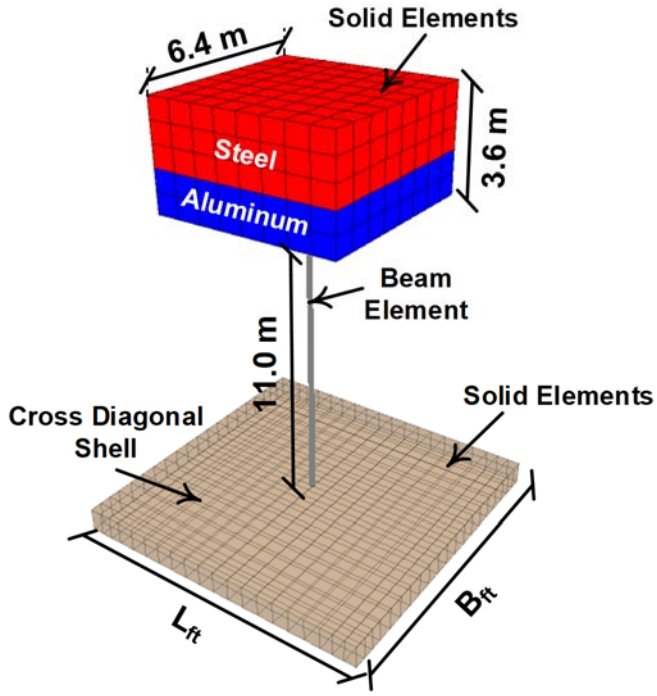

Fig. 5. Structural model configurations for MKH02 and MKH04.

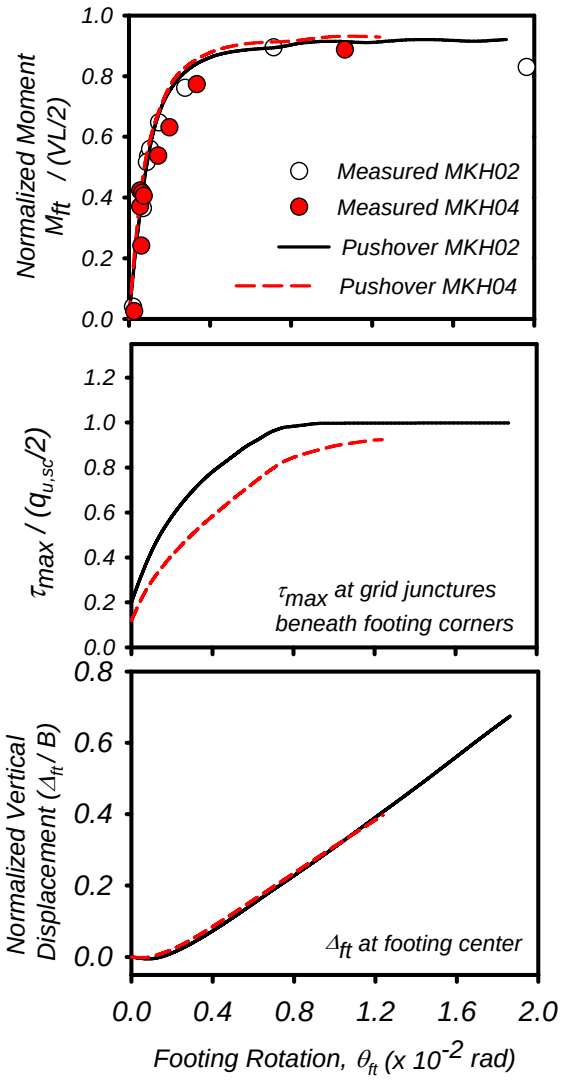

Fig. 6. Pushover responses for the structures on the embedded grids in MKH02 (A_r = 24%) and MKH04 (A_r = 33%): (a) normalized footing moment, (b) normalized maximum shear stress in the soil-cement at the top of the grid, and (c) normalized vertical displacement at the footing center.

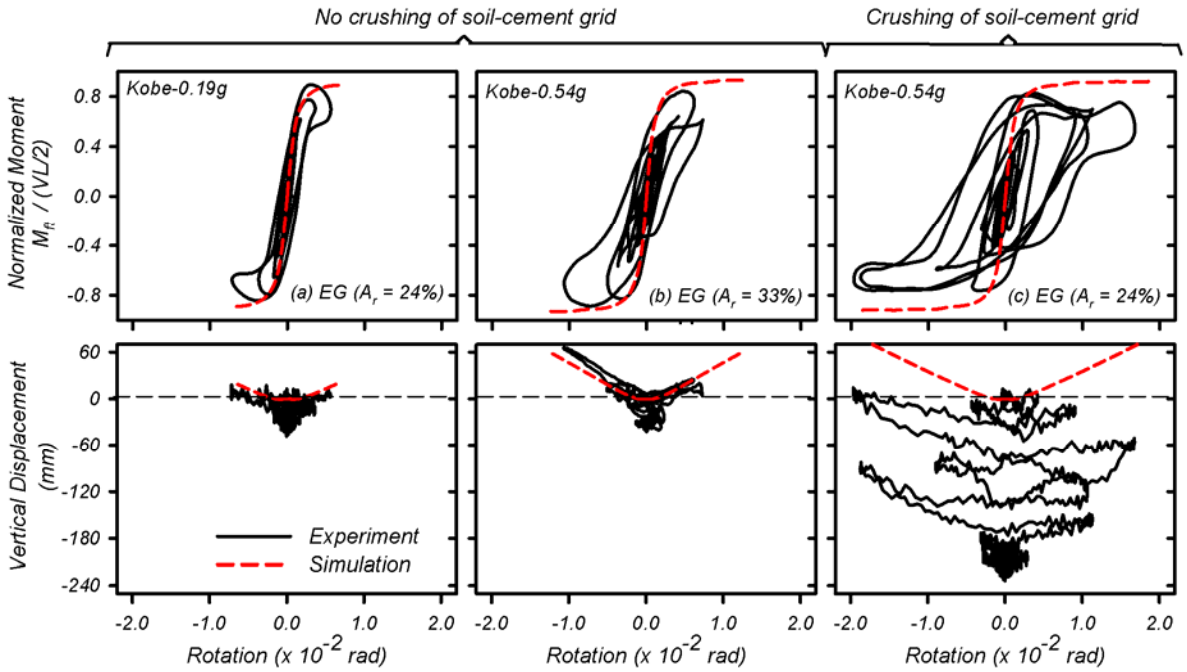

Fig. 7. Computed pushover and measured dynamic footing responses on embedded grids: (a) with A_r = 24% during Kobe motion with PBA = 0.19g; (b) with A_r = 33% during Kobe motion with PBA = 0.54g; and (c) with A_r = 24% during Kobe motion with PBA = 0.54g.

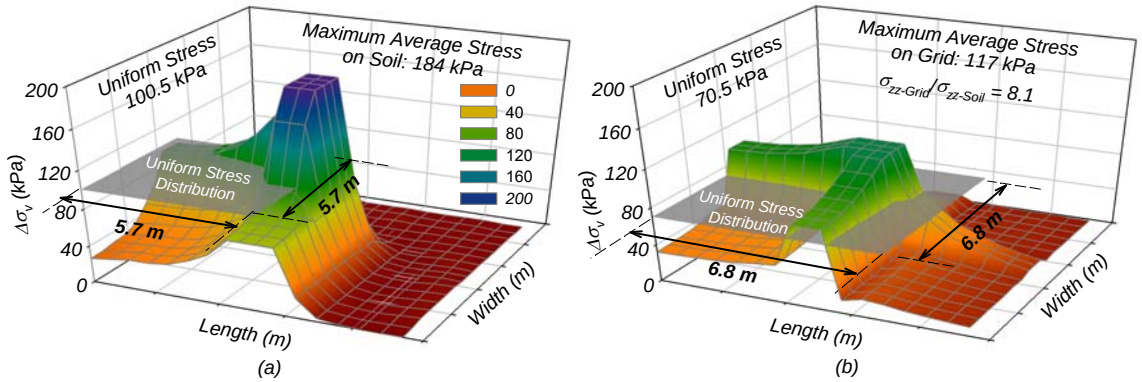

Fig. 8. Computed change in vertical stress due to the static structural load for the embedded grid with A_r = 24%: (a) change in vertical stress $\Delta\sigma_v$ at the base of the footing; and (b) change in vertical stress $\Delta\sigma_v$ on the surface of soil-cement grid (2.2 m below the footing base).

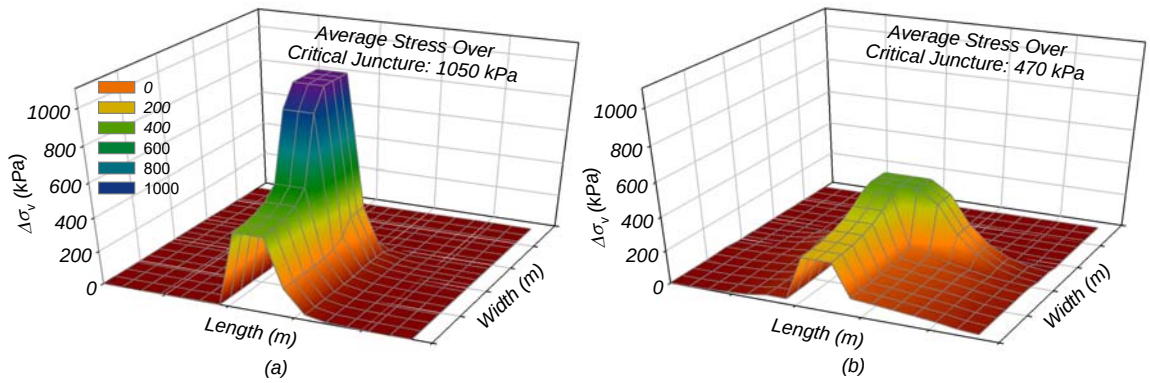

Fig. 9. Computed change in vertical stress for the embedded grid with A_r = 24% during foundation rocking at $\theta_{ft} \approx 0.006$ rad: (a) change in vertical stress $\Delta\sigma_v$ at the base of the footing; and (b) change in vertical stress $\Delta\sigma_v$ at the elevation of the top of the soil-cement grid (2.2 m below the footing base).

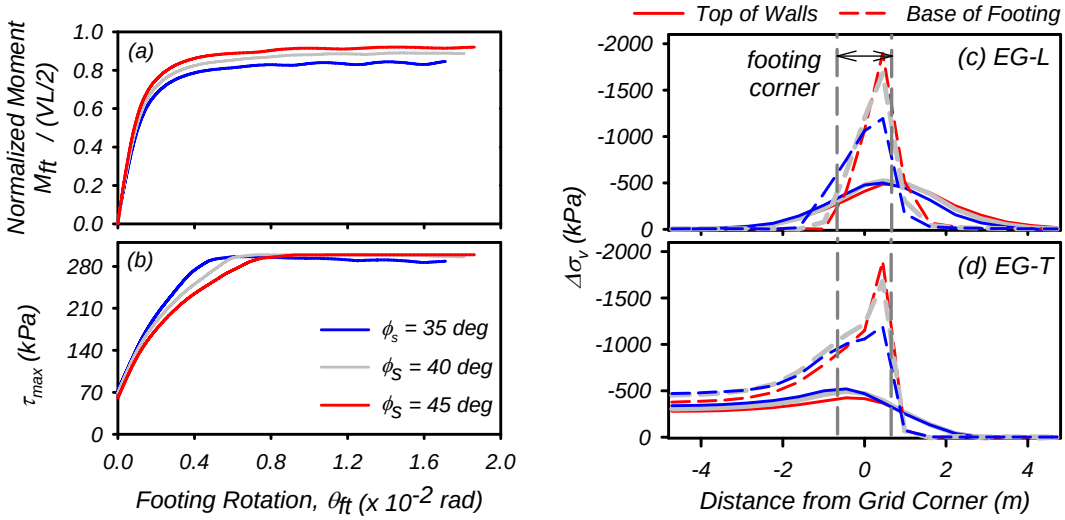

Fig. 10. Effect of the sand friction angle on the pushover response for the embedded grid with A_r = 24% and H_s = 2.2 m: (a) moment versus footing rotation, (b) maximum shear stress in the soil-cement versus footing rotation, (c) $\Delta\sigma_v$ at the base of the footing and top of the soil-cement grid along the longitudinal wall (EG-L), and (d) $\Delta\sigma_v$ at the base of the footing and top of the soil-cement grid along the transverse wall (EG-T).

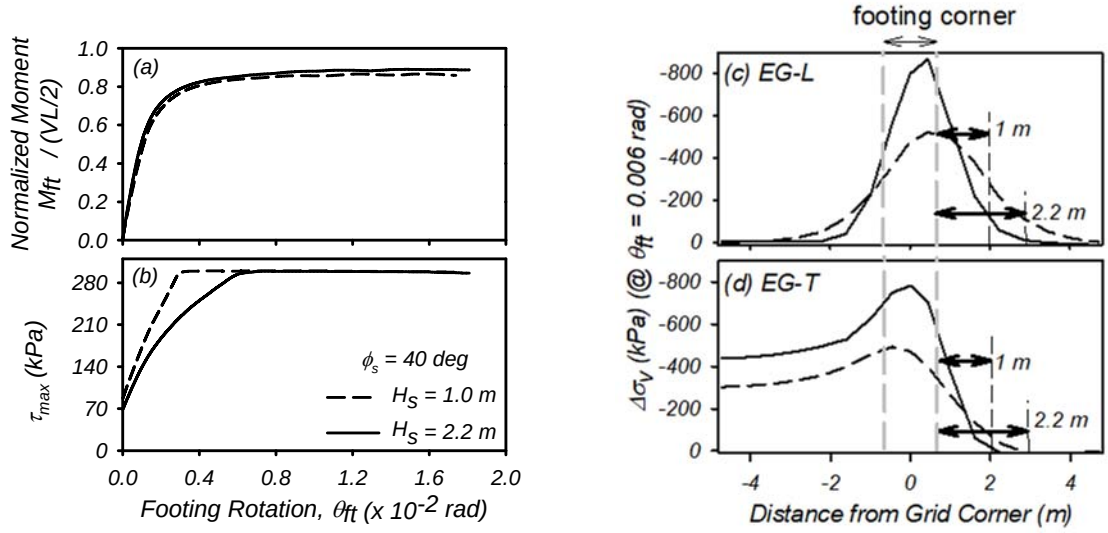

Fig. 11. Effect of top sand layer thickness on the pushover response for the embedded grid with A_r = 24%: (a) moment versus footing rotation, (b) maximum shear stress in the soil-cement versus footing rotation, (c) $\Delta\sigma_v$ along longitudinal wall (EG-L) at a footing rotation of 0.006 radians, and (d) $\Delta\sigma_v$ along transverse wall (EG-T) at a footing rotation of 0.006 radians

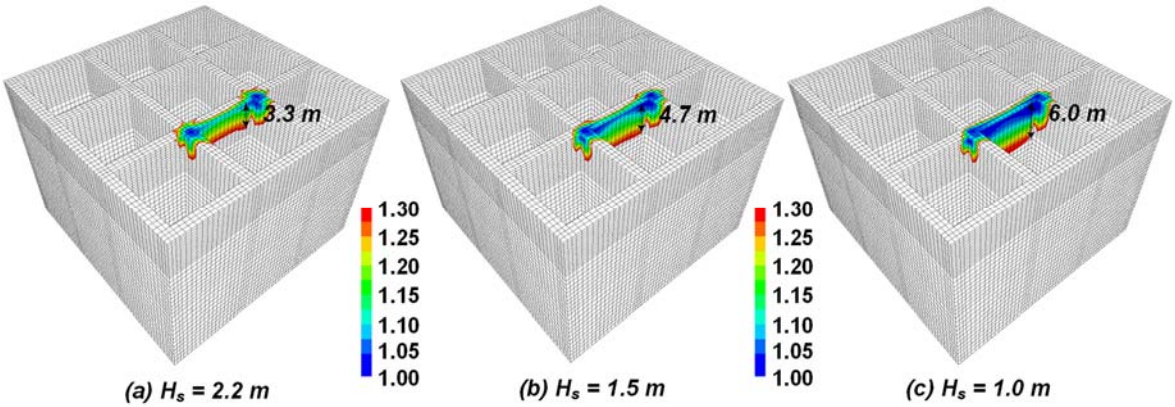

Fig. 12. Contours of the strength/stress ratio (where less than 1.3) for embedded grid with A_r = 24% under lateral loading to a footing rotation of 0.006 radians: (a) H_s = 2.2 m, (b) H_s = 1.5 m, and (c) H_s = 1.0 m.

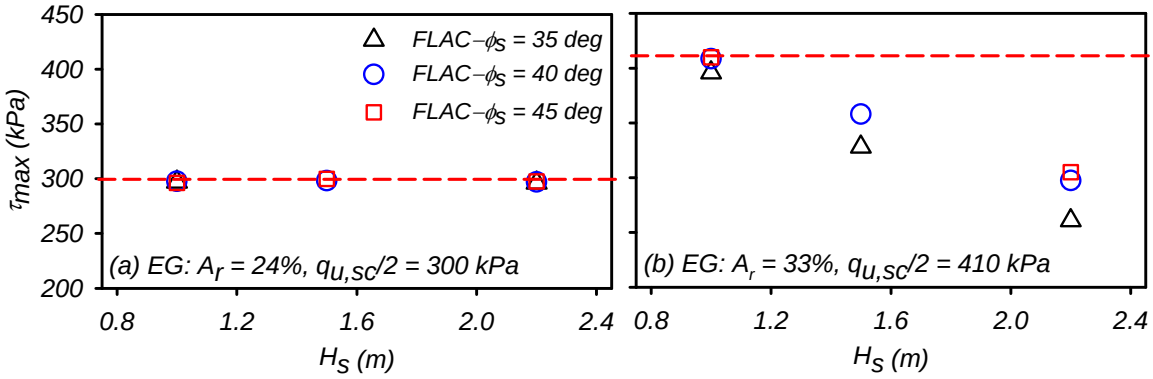

Fig. 13. Effect of sand layer thickness and sand friction angle on the maximum shear stresses in the critical juncture for: (a) the embedded grid with A_r = 24%, and (b) the embedded grid with A_r = 33%.

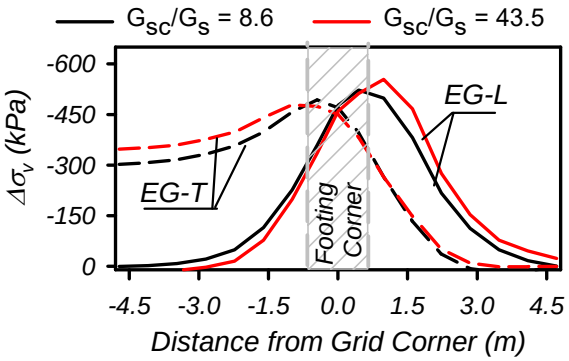

Fig. 14. Effect of the ratio of soil-cement stiffness (G_{sc}) to enclosed soil stiffness (G_s) on stresses in the embedded grid with A_r = 24% and H_s = 2.2 m during lateral loading.

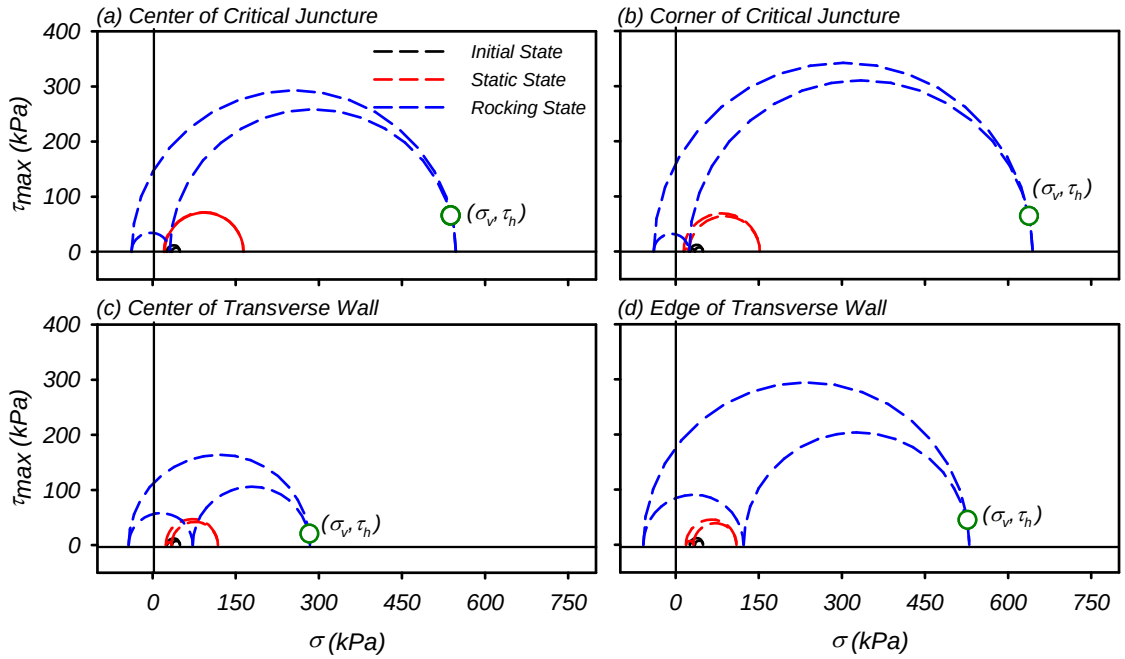

Figure 15. Mohr circles for the initial, static and rocking state of stresses in: (a) the middle zone in the critical juncture, (b) the most strongly loaded zone in the critical juncture, (c) the middle zone at the middle of the transverse wall (EG-T), and (d) the most strongly loaded zone at the middle of the transverse wall.

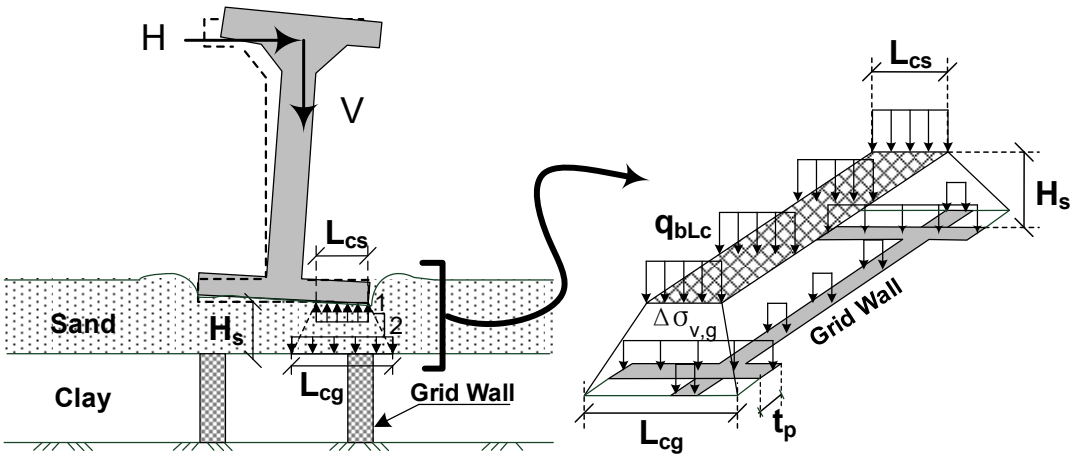

Fig. 16. Schematic of rocking foundation and 2:1 method for estimating vertical stresses imposed on the top of the soil-cement grid

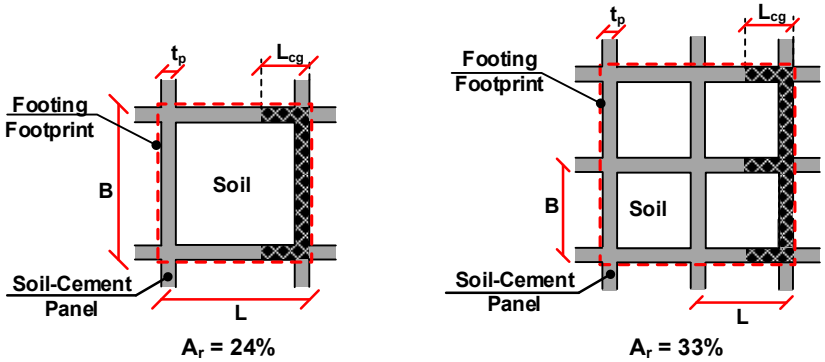

Fig. 17. Schematic of contact areas on the soil-cement grid during foundation rocking with rocking stresses controlled by arching directly onto the soil-cement grid

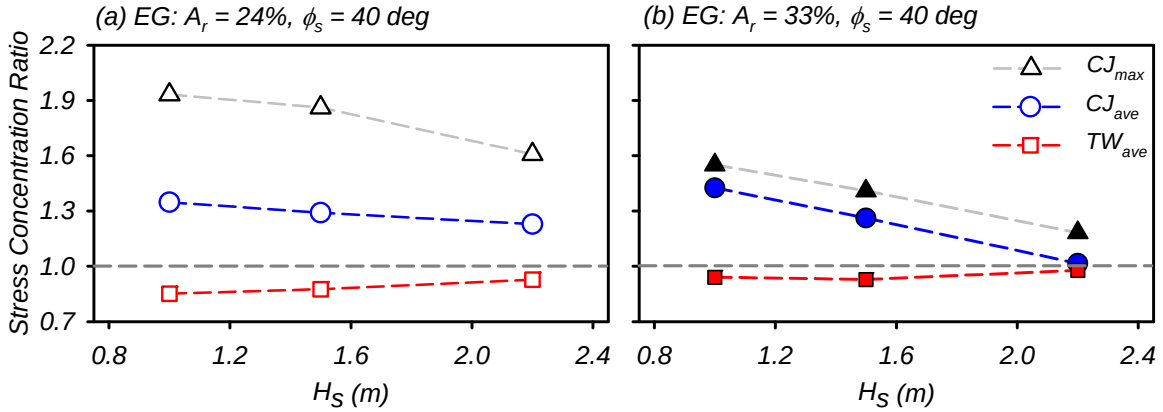

Fig. 18. Stress concentration ratios at different locations in the soil-cement grids beneath a rocking footing from analyses with elastic soil-cement grids: (a) the embedded grid with A_r = 24%, and (b) the embedded grid with A_r = 33%.

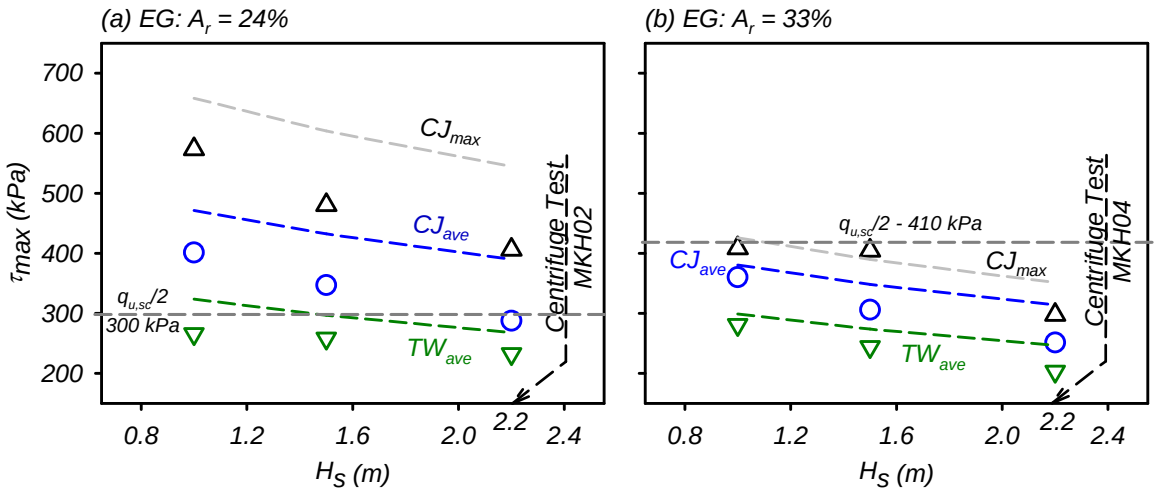

Fig. 19. Maximum and average maximum shear stress in the critical juncture (CJ_{max} and CJ_{ave}) and average maximum shear stress in the transverse wall (TW_{ave}) based on analytical (dashed lines) and 3D numerical (symbols) analyses with elastic soil-cement grids: (a) the embedded grid with A_r = 24%, and (b) the embedded grid with A_r = 33%.